Supporting Information for

Mapping Fast Tissue Dynamics With Long Camera Exposures Via Intensity Modulation

Hengfa Lu, Qingwei Fang, Jewel A. Ashbrook, Victoria Nemchek, Michela Fracassi, Theresa A. Jones and Andrew K. Dunn

To whom correspondence should be addressed.
E-mail: adunn@utexas.edu

This PDF file includes:

Supporting Information Text

S1. Derivation of SIMSI

Here, we provide a step-by-step derivation of the theoretical forward model for sinusoidal intensity modulation speckle imaging (SIMSI). We begin with the fundamental relationship between the measured speckle contrast and the intensity autocorrelation function, $g_2(\tau)$, and then derive the SIMSI forward model for (a) the practical case of finite-duration camera exposure and (b) the idealized large-exposure limit to build intuition.

A. Fundamentals and Notations. In speckle imaging, the relation between speckle contrast, $K(T)$, and pixel intensity autocorrelation function, $g_2(\tau)$, is formulated as follows (1, 2):

$$K^2(T) = \frac{2\langle I\rangle^2}{T^2\langle I_m\rangle^2}\int_0^T M(\tau)g_2(\tau)d\tau - 1, \quad [1]$$

where $I_m(t) = I(t)m(t)$ is the modulated signal intensity within the camera exposure, $I(t)$ is the stationary speckle intensity signal, $0 \le m(t) \le 1$ is the temporal modulation waveform applied within the camera exposure, and

$$M(\tau) = \int_0^{T-\tau} m(t)m(t+\tau)dt, \quad 0 \le \tau \le T, \quad [2]$$

is the finite-T autocorrelation of $m(t)$ over the exposure. Angle brackets $\langle\cdot\rangle$ denote an ensemble (or spatial) average. A subscript T denotes an explicit average over the exposure $\langle x\rangle_T \equiv \frac{1}{T}\int_0^T x(t)\,dt$.

In conventional (unmodulated) speckle imaging(3–5), the laser intensity is kept constant within each exposure, i.e., $m(t) = 1$ for $t \in [0, T]$, so $M(\tau) = T - \tau$, and $\langle I_m\rangle = \langle I\rangle$, Eq. (1) simplifies to the familiar form:

$$K^2(T) = \frac{2}{T^2}\int_0^T (T-\tau)g_2(\tau)d\tau - 1. \quad [3]$$

SIMSI introduces a sinusoidal modulation waveform within each exposure,

$$m(t) = \frac{1}{2} + \frac{1}{2}\cos(2\pi f_m t), \qquad f_m > 0 \text{ (Hz)}, \quad [4]$$

which satisfies $0 \le m(t) \le 1$ on $[0, T]$. The physical waveform seen by the camera is the time-gated product

$$h_T(t) = m(t)\, w_T^{\text{time}}(t), \qquad w_T^{\text{time}}(t) = \begin{cases} 1, & 0 \le t \le T, \\ 0, & \text{otherwise.} \end{cases} \quad [5]$$

The exposure-time mean of $m(t)$ is $\langle m\rangle_T = \frac{1}{T}\int_0^T m(t)\,dt$, hence

$$\langle I_m\rangle = \langle I\rangle\,\langle m\rangle_T. \quad [6]$$

When exposures contain an integer number of modulation periods, $\langle m\rangle_T = \frac{1}{2}$ and $\langle I_m\rangle = \frac{1}{2}\langle I\rangle$.

B. Practical Case: Finite Exposure. We start from Eq. (1) and convert the correlation integral to the frequency domain while keeping the finite upper limit T. Introduce the one-sided lag-domain window

$$w_T^{\text{lag}}(\tau) = \begin{cases} 1, & 0 \le \tau \le T, \\ 0, & \text{otherwise,} \end{cases} \qquad W_T^{\text{lag}}(f) = \int_0^T e^{-i2\pi f\tau}\,d\tau = T\,\text{sinc}(fT)\,e^{-i\pi fT}, \quad [7]$$

where $\text{sinc}(x) = \sin(\pi x)/\pi x$ and $\text{sinc}(0) = 1$. Hence, Eq. (1) can be equivalently written:

$$K^2(T) = \frac{2\langle I\rangle^2}{T^2\langle I_m\rangle^2}\int_0^T M(\tau)g_2(\tau)d\tau - 1 = \frac{2\langle I\rangle^2}{T^2\,\langle I_m\rangle^2}\int_{-\infty}^{\infty} w_T^{\text{lag}}(\tau)M(\tau)g_2(\tau)\,d\tau - 1. \quad [8]$$

Using the identity

$$\int_{-\infty}^{\infty} a(\tau)\,b(\tau)\,d\tau = \mathcal{F}\{a\} \otimes \mathcal{F}\{b\}\big|_{f=0}, \quad [9]$$

and applying it twice yields

$$\int_{-\infty}^{\infty} w_T^{\text{lag}}(\tau)M(\tau)g_2(\tau)\,d\tau = \left(W_T^{\text{lag}} \otimes \mathcal{P}_m \otimes \mathcal{P}_I\right)\big|_{f=0}, \quad [10]$$

where $\mathcal{P}_m(f) = \mathcal{F}\{M\}(f)$ and $\mathcal{P}_I(f) = \mathcal{F}\{g_2\}(f)$.

Relating $\mathcal{P}_m$ to the within-exposure modulation via Wiener–Khinchin. The within-exposure modulation (defined in Eq. (5)) is

$$h_T(t) = m(t)\, w_T^{\text{time}}(t), \qquad w_T^{\text{time}}(t) = \mathbf{1}_{[0,T]}(t).$$

Let $H_T(f) = \mathcal{F}\{h_T\}(f)$. Since $M(\tau)$ in Eq. (1) is the autocorrelation of $h_T(t)$ over the exposure, the energy version of Wiener–Khinchin gives

$$\mathcal{P}_m(f) = \mathcal{F}\{M\}(f) = |H_T(f)|^2. \tag{11}$$

Writing the triple convolution in Eq. (10) at $f = 0$,

$$\begin{aligned} W_T^{\text{lag}} \otimes \mathcal{P}_m \otimes \mathcal{P}_I\big|_{f=0} &= \iint_{-\infty}^{\infty} W_T^{\text{lag}}\big(-(f_1+f_2)\big)\, \mathcal{P}_m(f_1)\, \mathcal{P}_I(f_2) df_1 df_2 \\ &= \iint \left[\int_0^T e^{\,i2\pi(f_1+f_2)\tau}\, d\tau\right] \mathcal{P}_m(f_1)\, \mathcal{P}_I(f_2) df_1 df_2 \\ &= \int_0^T \left[\int e^{\,i2\pi f_1\tau} \mathcal{P}_m(f_1)\, df_1\right] \left[\int e^{\,i2\pi f_2\tau} \mathcal{P}_I(f_2)\, df_2\right] d\tau \\ &= \int_0^T M(\tau)\, g_2(\tau)\, d\tau, \end{aligned} \tag{12}$$

where we used inverse Fourier transforms in the inner brackets. Since $M(\tau)$ and $g_2(\tau)$ are even and $M(\tau)$ is supported on $[-T, T]$,

$$\int_0^T M(\tau)\, g_2(\tau)\, d\tau = \tfrac{1}{2} \int_{-\infty}^{\infty} M(\tau)\, g_2(\tau)\, d\tau. \tag{13}$$

Applying Parseval/Plancherel theorem,

$$\int_{-\infty}^{\infty} M(\tau)\, g_2(\tau)\, d\tau = \int_{-\infty}^{\infty} \mathcal{P}_m(f)\, \mathcal{P}_I(f)\, df = \int_{-\infty}^{\infty} |H_T(f)|^2\, \mathcal{P}_I(f)\, df. \tag{14}$$

Combining Eq. (8)–Eq. (14) gives the exact finite-exposure forward model:

$$K^2(T, f_m) = \frac{\langle I \rangle^2}{T^2\, \langle I_m \rangle^2} \int_{-\infty}^{\infty} \big|H_T(f)\big|^2\, \mathcal{P}_I(f)\, df - 1. \tag{15}$$

Explicit kernels for SIMSI. Next, we make $|H_T(f)|^2$ explicit. Using

$$H_T(f) = \mathcal{F}\{m(t)\} \otimes \mathcal{F}\{w_T^{\text{time}}(t)\}, \qquad \mathcal{F}\{w_T^{\text{time}}(t)\}(f) = T\, \operatorname{sinc}(fT)\, e^{-i\pi fT}, \tag{16}$$

and, for SIMSI,

$$\mathcal{F}\{m(t)\}(f) = \frac{1}{2}\, \delta(f) + \frac{1}{4}\, \delta(f - f_m) + \frac{1}{4}\, \delta(f + f_m), \tag{17}$$

we obtain

$$H_T(f) = \left(\frac{1}{2}\, \delta(f) + \frac{1}{4}\, \delta(f - f_m) + \frac{1}{4}\, \delta(f + f_m)\right) \otimes \left(T\, \operatorname{sinc}(fT)\, e^{-i\pi fT}\right) = A_0(f) + A_+(f) + A_-(f), \tag{18}$$

where

$$\begin{aligned} A_0(f) &\equiv \frac{T}{2}\, \operatorname{sinc}(fT)\, e^{-i\pi fT}, \\ A_+(f) &\equiv \frac{T}{4}\, \operatorname{sinc}\big((f - f_m)T\big)\, e^{-i\pi(f-f_m)T}, \\ A_-(f) &\equiv \frac{T}{4}\, \operatorname{sinc}\big((f + f_m)T\big)\, e^{-i\pi(f+f_m)T}. \end{aligned} \tag{19}$$

Performing direct expansion, we have

$$|H_T(f)|^2 = |A_0|^2 + |A_+|^2 + |A_-|^2 \; + \; 2\Re\big(A_0 A_+^* + A_0 A_-^* + A_+ A_-^*\big). \tag{20}$$

The auto terms are

$$|A_0|^2 = \frac{T^2}{4}\, \operatorname{sinc}^2(fT), \qquad |A_+|^2 = \frac{T^2}{16}\, \operatorname{sinc}^2\big((f - f_m)T\big), \qquad |A_-|^2 = \frac{T^2}{16}\, \operatorname{sinc}^2\big((f + f_m)T\big). \tag{21}$$

Importantly, each cross term carries a constant phase:

$$
\begin{aligned}
A_0 A_+^* &= \frac{T^2}{8}\,\mathrm{sinc}(fT)\,\mathrm{sinc}\big((f-f_m)T\big)\,e^{-i\pi fT}\,e^{+i\pi(f-f_m)T} = \frac{T^2}{8}\,\mathrm{sinc}(fT)\,\mathrm{sinc}\big((f-f_m)T\big)\,e^{-i\pi f_m T},\\
A_0 A_-^* &= \frac{T^2}{8}\,\mathrm{sinc}(fT)\,\mathrm{sinc}\big((f+f_m)T\big)\,e^{-i\pi fT}\,e^{+i\pi(f+f_m)T} = \frac{T^2}{8}\,\mathrm{sinc}(fT)\,\mathrm{sinc}\big((f+f_m)T\big)\,e^{+i\pi f_m T},\\
A_+ A_-^* &= \frac{T^2}{16}\,\mathrm{sinc}\big((f-f_m)T\big)\,\mathrm{sinc}\big((f+f_m)T\big)\,e^{-i\pi(f-f_m)T}\,e^{+i\pi(f+f_m)T}\\
&= \frac{T^2}{16}\,\mathrm{sinc}\big((f-f_m)T\big)\,\mathrm{sinc}\big((f+f_m)T\big)\,e^{+i2\pi f_m T}.
\end{aligned}
\tag{22}
$$

Taking real parts,

$$
\begin{aligned}
\frac{|H_T(f)|^2}{T^2} = {}& \frac{1}{4}\,\mathrm{sinc}^2(fT) + \frac{1}{16}\,\mathrm{sinc}^2\big((f-f_m)T\big) + \frac{1}{16}\,\mathrm{sinc}^2\big((f+f_m)T\big)\\
&+ \frac{1}{4}\cos(\pi f_m T)\,\mathrm{sinc}(fT)\,\mathrm{sinc}\big((f-f_m)T\big)\\
&+ \frac{1}{4}\cos(\pi f_m T)\,\mathrm{sinc}(fT)\,\mathrm{sinc}\big((f+f_m)T\big)\\
&+ \frac{1}{8}\cos(2\pi f_m T)\,\mathrm{sinc}\big((f-f_m)T\big)\,\mathrm{sinc}\big((f+f_m)T\big).
\end{aligned}
\tag{23}
$$

The auto-kernels that remain under the resolved-lobe or integer-cycle conditions are plotted in Fig. S1B. Substituting into Eq. (15) gives

$$
\begin{aligned}
K^2(T,f_m) = {}& \frac{\langle I\rangle^2}{\langle I_m\rangle^2}\int \mathcal{P}_I(f)\left[\frac{1}{4}\,\mathrm{sinc}^2(fT) + \frac{1}{16}\,\mathrm{sinc}^2\big((f-f_m)T\big) + \frac{1}{16}\,\mathrm{sinc}^2\big((f+f_m)T\big)\right] df\\
&+ \frac{\langle I\rangle^2}{\langle I_m\rangle^2}\int \mathcal{P}_I(f)\left[\frac{1}{4}\cos(\pi f_m T)\,\mathrm{sinc}(fT)\,\mathrm{sinc}\big((f-f_m)T\big)\right] df\\
&+ \frac{\langle I\rangle^2}{\langle I_m\rangle^2}\int \mathcal{P}_I(f)\left[\frac{1}{4}\cos(\pi f_m T)\,\mathrm{sinc}(fT)\,\mathrm{sinc}\big((f+f_m)T\big)\right] df\\
&+ \frac{\langle I\rangle^2}{\langle I_m\rangle^2}\int \mathcal{P}_I(f)\left[\frac{1}{8}\cos(2\pi f_m T)\,\mathrm{sinc}\big((f-f_m)T\big)\,\mathrm{sinc}\big((f+f_m)T\big)\right] df\\
&- 1.
\end{aligned}
\tag{24}
$$

Each cross term in Eq. (24) has the generic form

$$
\mathcal{C}_{a,b} = \int_{-\infty}^{\infty} \mathcal{P}_I(f)\,\mathrm{sinc}((f-a)T)\,\mathrm{sinc}((f-b)T)df, \qquad (a,b)\in\{(0,\pm f_m),(f_m,-f_m)\},
\tag{25}
$$

multiplied by constant phase factors $\cos(\pi f_m T)$ or $\cos(2\pi f_m T)$. The central question is how large $\mathcal{C}_{a,b}$ can be relative to the auto-kernel terms.

Exact overlap identity. Using $\mathrm{sinc}(x) = \sin(\pi x)/(\pi x)$, set $u = (f-a)T$ so that $df = du/T$ and $(f-b)T = u + \Delta$ with $\Delta = (a-b)T$. Then

$$
\int_{-\infty}^{\infty} \mathrm{sinc}\big((f-a)T\big)\,\mathrm{sinc}\big((f-b)T\big)df = \frac{1}{T}\int_{-\infty}^{\infty} \mathrm{sinc}(u)\,\mathrm{sinc}(u+\Delta)du.
\tag{26}
$$

Using the Fourier pair $\mathrm{rect}(t/T) \iff T\,\mathrm{sinc}(fT)$ and Parseval/Wiener–Khinchin for autocorrelation, we get

$$
\int \mathrm{sinc}(u)\,\mathrm{sinc}(u+\Delta)\,du = \int \mathrm{rect}(f)\,e^{i2\pi f\Delta}\,\mathrm{rect}(f)\,df = \int_{-1/2}^{1/2} e^{i2\pi f\Delta}\,df = \frac{\sin(\pi\Delta)}{\pi\Delta} = \mathrm{sinc}\big(\Delta\big).
\tag{27}
$$

Thus, we obtain the overlap identity

$$
\int_{-\infty}^{\infty} \mathrm{sinc}\big((f-a)T\big)\,\mathrm{sinc}\big((f-b)T\big)\,df = \frac{1}{T}\,\mathrm{sinc}\big((a-b)T\big),
\tag{28}
$$

Since $|\mathrm{sinc}(x)| \le \min\{1, 1/(\pi|x|)\}$, the overlap is small when $|a-b|T \gg 1$ (spectrally resolved lobes).

Cross–term estimates. The three cross terms in Eq. (24) can be written in the generic form Eq. (25). The magnitude of $\mathcal{C}_{a,b}$ is governed by the geometric overlap of the two lobes. The exact overlap identity Eq. (28) shows that the lobe overlap already decays as $1/T$ and vanishes whenever $f_m T \in \mathbb{Z}$ for the pairs in Eq. (25). We now provide a uniform, assumption–free bound that depends only on spectral separation.

Uniform (sup-norm) bound. Assume $\mathcal{P}_I$ is bounded, $\|\mathcal{P}_I\|_\infty < \infty$. Starting from Eq. (25), apply the triangle inequality and then change variables $u = (f-a)T$ (so $df = du/T$ and $(f-b)T = u + \Delta$ with $\Delta = (a-b)T$):

$$\begin{aligned} |\mathcal{C}_{a,b}| &\le \|\mathcal{P}_I\|_\infty \int_{-\infty}^{\infty} \left|\operatorname{sinc}\big((f-a)T\big)\,\operatorname{sinc}\big((f-b)T\big)\right| df \\ &= \frac{\|\mathcal{P}_I\|_\infty}{T} \int_{-\infty}^{\infty} \left|\operatorname{sinc}(u)\,\operatorname{sinc}(u+\Delta)\right| du. \end{aligned} \tag{29}$$

Using the Cauchy–Schwarz inequality together with the exact overlap identity in Eq. (28), we obtain

$$\int \left|\operatorname{sinc}(u)\,\operatorname{sinc}(u+\Delta)\right| du \le \left(\int \operatorname{sinc}^2(u)\,du\right)^{1/2}\left(\int \operatorname{sinc}^2(u+\Delta)\,du\right)^{1/2} = \int \operatorname{sinc}^2(u)\,du = 1, \tag{30}$$

and combining Eq. (29)-Eq. (30),

$$|\mathcal{C}_{a,b}| \le \frac{\|\mathcal{P}_I\|_\infty}{T}. \tag{31}$$

A sharper, separation–dependent estimate follows by writing

$$|\operatorname{sinc}(u)\operatorname{sinc}(u+\Delta)| \le \min\left\{\operatorname{sinc}^2(u),\ \frac{1}{\pi|u+\Delta|}\operatorname{sinc}(u)\right\}$$

and splitting the u–integral at $|u+\Delta| = 1$; this yields

$$\int \left|\operatorname{sinc}(u)\operatorname{sinc}(u+\Delta)\right| du \le \frac{c_0}{1+|\Delta|}, \qquad \text{with } c_0 = \frac{1}{\pi}\int_{-\infty}^{\infty}\operatorname{sinc}(u)\,du = \frac{1}{\pi}. \tag{32}$$

Hence, for spectrally resolved lobes ($|a-b|T = |\Delta| \gg 1$),

$$|\mathcal{C}_{a,b}| \le \frac{\|\mathcal{P}_I\|_\infty}{\pi\,|a-b|\,T^2}, \qquad (|a-b|T \gg 1). \tag{33}$$

In particular, for the SIMSI pairs $(a,b) \in \{(0,\pm f_m),(f_m,-f_m)\}$,

$$\left|\mathcal{C}_{0,\pm f_m}\right| \lesssim \frac{\|\mathcal{P}_I\|_\infty}{\pi f_m T^2}, \qquad \left|\mathcal{C}_{f_m,-f_m}\right| \lesssim \frac{\|\mathcal{P}_I\|_\infty}{2\pi f_m T^2}, \qquad (f_m T \gg 1), \tag{34}$$

Equations (31)–(34) show that cross terms are uniformly $\mathcal{O}(1/T)$ and, when lobes are separated by $|a-b| \gtrsim 1/T$, they decay as $\mathcal{O}(1/(|a-b|T^2))$, independently of $\mathcal{P}_I$.

Practical criteria and the integer-cycle case. The auto-kernels in Eq. (24) integrate to areas $1/(4T)$ (DC) and $1/(16T)$ (each side lobe), so the total auto-area is $(3/8)/T$. In contrast, Eq. (34) shows cross terms scale as $\mathcal{O}(1/T^2)$ once $f_m T \gg 1$, and are therefore negligible at large T even before accounting for the small $\operatorname{sinc}((a-b)T)$ factors.

A simple sufficient rule is

$$f_m T \gtrsim 3 \quad\Longrightarrow\quad |\operatorname{sinc}(f_m T)| \lesssim 0.1,\ \ |\operatorname{sinc}(2 f_m T)| \lesssim 0.05, \tag{35}$$

under which cross-term integrals are much smaller than the auto-term integrals. Most importantly, when the exposure contains an integer number of modulation cycles,

$$f_m T \in \mathbb{Z} \quad\Longrightarrow\quad \operatorname{sinc}(f_m T) = \operatorname{sinc}(2 f_m T) = 0, \tag{36}$$

and all three overlaps in Eq. (25) are strongly suppressed and negligible under our conditions, independently of $\mathcal{P}_I$. The constant phase factors in Eq. (24) then multiply zero and are immaterial.

Compact forward model (resolved lobes or integer cycles). When the cross terms are negligible (in particular, for $f_m T \in \mathbb{Z}$), evenness of $\mathcal{P}_I$ and sinc^2 allows combining the $\pm f_m$ lobes:

$$K^2(T, f_m) = \frac{\langle I\rangle^2}{\langle I_m\rangle^2}\int_{-\infty}^{\infty}\mathcal{P}_I(f)\left[\frac{1}{4}\operatorname{sinc}^2(fT) + \frac{1}{8}\operatorname{sinc}^2\big((f-f_m)T\big)\right] df - 1. \tag{37}$$

When the exposure contains an integer number of modulation periods, $\langle m\rangle_T = \frac{1}{2}$ and $\langle I_m\rangle = \frac{1}{2}\langle I\rangle$, giving

$$\boxed{\begin{aligned} K^2(T, f_m) &= \int_{-\infty}^{\infty}\mathcal{P}_I(f)\left[\operatorname{sinc}^2(fT) + \frac{1}{2}\operatorname{sinc}^2\big((f-f_m)T\big)\right] df - 1, \\ &= \int_{-\infty}^{\infty}\mathcal{P}_I(f)\operatorname{sinc}^2(fT) df + \frac{1}{2}\int_{-\infty}^{\infty}\mathcal{P}_I(f)\operatorname{sinc}^2\big((f-f_m)T\big) df - 1. \end{aligned}} \tag{38}$$

Numerical examples using this expression are shown in Fig. S1C.

In this work, we used $T = 40\,\text{ms}$ and

$$f_m \in \{25, 50, 100, 150, 200, 300, 400, 800, 1600, 3200, 6400, 12800, 25600, 51200, 100000\}\ \text{Hz}.$$

so $f_m T \in \mathbb{Z}$ for every f_m. Therefore, the cross terms in Eq. (24) vanish exactly, and Eq. (38) holds without approximation for all data reported in the manuscript.

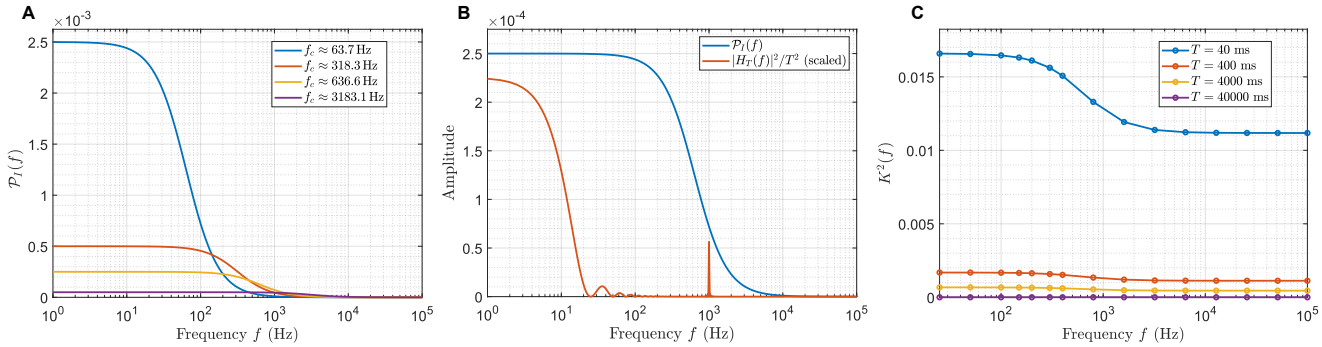

Fig. S1. Frequency-domain interpretation of SIMSI. **(A)** Representative $\mathcal{P}_I(f)$ generated from a Lorentzian field model with different correlation times; **(B)** SIMSI sampling kernel for exposure $T = 40$ ms and modulation $f_m = 1000$ Hz; **(C)** Predicted speckle contrast $K^2(T, f_m)$ versus f_m for several T, evaluated with the compact forward model in Eq. (38); K^2 decreases approximately as $1/T$ and flattens at high f_m as the sampling window moves beyond the PSD roll-off. Cross terms vanish for integer-cycle exposures ($f_m T \in \mathbb{Z}$) and are negligible when $f_m T \gg 1$.

C. The Ideal Case: Large-Exposure Limit. The finite-exposure forward model in Eq. (24) shows that $K^2(T, f_m)$ is an average of $\mathcal{P}_I(f)$ through three sinc^2 kernels centered at $f = 0$ and $f = \pm f_m$, plus cross terms. As the exposure increases ($T \to \infty$), each kernel becomes a narrow window that samples the PSD at its center, and the overall contrast scales as $1/T$.

Recall the exact PSD form and its kernel decomposition:

$$K^2(T, f_m) = \frac{\langle I \rangle^2}{T^2 \langle I_m \rangle^2} \int_{-\infty}^{\infty} |H_T(f)|^2 \, \mathcal{P}_I(f) \, df - 1, \tag{39}$$

$$\frac{|H_T(f)|^2}{T^2} = \underbrace{\frac{1}{4}\,\mathrm{sinc}^2(fT) + \frac{1}{16}\,\mathrm{sinc}^2((f - f_m)T) + \frac{1}{16}\,\mathrm{sinc}^2((f + f_m)T)}_{\text{three auto kernels}} + \underbrace{\mathsf{X}_T(f)}_{\text{cross terms}}. \tag{40}$$

with $\mathrm{sinc}(x) = \sin(\pi x)/(\pi x)$.

Auto-kernel asymptotics. For any bounded, continuous F, when $T \to \infty$,

$$\lim_{T\to\infty} T \int_{-\infty}^{\infty} F(f)\,\mathrm{sinc}^2\big((f - f_0)T\big)\, df = F(f_0). \tag{41}$$

Applying Eq. (41) to the three auto kernels in Eq. (40) and using evenness of $\mathcal{P}_I(f)$ gives

$$\lim_{T\to\infty} T \int_{-\infty}^{\infty} \frac{|H_T(f)|^2}{T^2} \mathcal{P}_I(f)\, df = \frac{1}{4}\,\mathcal{P}_I(0) + \frac{1}{8}\mathcal{P}_I(f_m), \tag{42}$$

assuming cross terms vanish in the limit.

Cross-term limits. Each cross term in $\mathsf{X}_T(f)$ is an integral of a product of two shifted sinc lobes, e.g.,

$$\int \mathcal{P}_I(f)\ \mathrm{sinc}(fT)\ \mathrm{sinc}\big((f - f_m)T\big)\, df.$$

Using the exact overlap identity

$$\int \mathrm{sinc}((f - a)T)\ \mathrm{sinc}((f - b)T)\, df = \frac{1}{T}\,\mathrm{sinc}((a - b)T),$$

together with $|\mathrm{sinc}(x)| \le 1/(\pi|x|)$ for $|x| \ge 1$, shows that if the lobes are spectrally resolved ($|a - b|T \to \infty$) then

$$T \int \mathcal{P}_I(f)\ \mathrm{sinc}\big((f - a)T\big)\ \mathrm{sinc}\ \big((f - b)T\big)\, df \longrightarrow 0,$$

so the cross-term contribution is negligible in the large-T limit. In particular, if the exposure contains an integer number of modulation cycles ($f_m T \in \mathbb{Z}$), then $\mathrm{sinc}(f_m T) = \mathrm{sinc}(2 f_m T) = 0$ and all cross terms are exactly zero for any T.

Large-T sampling form. Combining Eq. (39)-Eq. (42) yields

$$\lim_{T\to\infty} T\frac{\langle I_m\rangle^2}{\langle I\rangle^2}\big(K^2(T,f_m)+1\big) = \frac{1}{4}\,\mathcal{P}_I(0) + \frac{1}{8}\,\mathcal{P}_I(f_m). \tag{43}$$

Equivalently, for large T,

$$K^2(T,f_m) \sim \frac{\langle I\rangle^2}{\langle I_m\rangle^2}\frac{1}{T}\left[\frac{1}{4}\mathcal{P}_I(0) + \frac{1}{8}\,\mathcal{P}_I(f_m)\right] - 1, \qquad T\to\infty. \tag{44}$$

When the exposure contains an integer number of modulation periods, $\langle m\rangle_T = \frac{1}{2}$ and $\langle I_m\rangle = \frac{1}{2}\langle I\rangle$, so $\langle I\rangle^2/\langle I_m\rangle^2 = 4$. In this case,

$$\lim_{T\to\infty} T\big(K^2(T,f_m)+1\big) = \mathcal{P}_I(0) + \frac{1}{2}\mathcal{P}_I(f_m), \qquad f_m T\in\mathbb{Z}. \tag{45}$$

Equivalently, for large T under $f_m T\in\mathbb{Z}$,

$$\boxed{K^2(T,f_m) \sim \frac{1}{T}\left[\mathcal{P}_I(0) + \frac{1}{2}\mathcal{P}_I(f_m)\right] - 1,} \tag{46}$$

which shows that the three sinc^2 kernels act as sampling windows of area $1/T$ centered at 0 and $\pm f_m$. This sampling picture is illustrated empirically in Fig. S1 B–C. K^2 decays as $1/T$, and in the limit SIMSI effectively samples $\mathcal{P}_I(f)$ at $f=0$ and $f=f_m$ with relative weights 1 and 1/2.

S2. Physics-informed, label-free parameter estimation for SIMSI

This section summarizes the parameter-estimation procedure used to recover spatial maps of PSD parameters from SIMSI measurements. Given $\widehat{K}^2(T, f_m)$ acquired at a finite set of modulation frequencies $\{f_{m,\ell}\}_{\ell=1}^{L}$, the goal is to infer parameter maps $\{a(\mathbf{r}),\, b(\mathbf{r}),\, \gamma(\mathbf{r}),\, f_c(\mathbf{r})\}$, where $\mathbf{r}$ denotes spatial location.

S2.1. Forward model and PSD parameterization. SIMSI measurements are related to the intensity-fluctuation PSD $\mathcal{P}_I(f)$ through the SIMSI measurement operator derived in Supplementary Note S1. In this work, we parameterize $\mathcal{P}_I(f)$ as

$$\mathcal{P}_I(f; a, b, \gamma, f_c) = a\Big(1 + (f/f_c)^{\gamma}\Big)^{-1} + b, \qquad a \geq 0,\ b \geq 0,\ \gamma > 0,\ f_c > 0, \tag{47}$$

where a sets the low-frequency amplitude, b captures an additive floor, γ controls the roll-off steepness, and f_c sets the characteristic frequency scale.

Given (a, b, γ, f_c), predicted SIMSI measurements at exposure time T and modulation frequencies $\{f_{m,\ell}\}_{\ell=1}^{L}$ are obtained by evaluating the analytical SIMSI model from Supplementary Note S1 under Eq. (47). We denote this synthesis mapping by

$$\mathbf{K}^2_{\mathrm{SIMSI}}(T;\, a, b, \gamma, f_c) = \Big[K^2_{\mathrm{SIMSI}}(T, f_{m,1}; a, b, \gamma, f_c), \ldots, K^2_{\mathrm{SIMSI}}(T, f_{m,L}; a, b, \gamma, f_c)\Big]^{\top} \in \mathbb{R}^L. \tag{48}$$

S2.2. Analysis-by-synthesis inverse mapping. We estimate parameters using a physics-informed, label-free analysis-by-synthesis framework that we previously introduced and validated for MESI parameter mapping, and here adapt to SIMSI by substituting the SIMSI forward model Eq. (48) as the synthesis layer (see (6)).

Let $\widehat{\mathbf{K}}^2_p = [\widehat{K}^2_p(T, f_{m,1}), \ldots, \widehat{K}^2_p(T, f_{m,L})]^{\top} \in \mathbb{R}^L$ denote the SIMSI measurements at pixel p. We learn a globally shared inverse operator $E_{\boldsymbol{\phi}} : \mathbb{R}^L \to \mathbb{R}^4$ parameterized by weights $\boldsymbol{\phi}$, implemented with a compact neural network. For numerical stability and to enforce positivity of f_c, the network predicts $s_p = \log_{10}(f_{c,p})$:

$$(a_p,\, b_p,\, \gamma_p,\, s_p) = E_{\boldsymbol{\phi}}\Big(\widehat{\mathbf{K}}^2_p\Big), \qquad f_{c,p} = 10^{s_p}. \tag{49}$$

The predicted parameters are then passed through the fixed SIMSI forward model to re-synthesize the measurements:

$$\widetilde{\mathbf{K}}^2_p(\boldsymbol{\phi}) = \mathbf{K}^2_{\mathrm{SIMSI}}(T;\, a_p, b_p, \gamma_p, 10^{s_p}) \in \mathbb{R}^L. \tag{50}$$

Training minimizes a reconstruction loss between measured and re-synthesized curves:

$$\boldsymbol{\phi}^* = \arg\min_{\boldsymbol{\phi}} \sum_{p} \mathcal{L}\Big(\widehat{\mathbf{K}}^2_p,\, \widetilde{\mathbf{K}}^2_p(\boldsymbol{\phi})\Big), \tag{51}$$

where we use a log-domain mean-squared error to emphasize relative errors across the dynamic range:

$$\mathcal{L}(\mathbf{u}, \mathbf{v}) = \frac{1}{L}\sum_{\ell=1}^{L} \big(\log(u_\ell + \epsilon) - \log(v_\ell + \epsilon)\big)^2, \qquad \epsilon > 0. \tag{52}$$

S2.3. Parameter constraints and practical settings. All four PSD parameters are estimated at every pixel. The exponent γ is estimated jointly with s (and hence f_c) under explicit bounds, reflecting that γ and f_c together determine the PSD roll-off in Eq. (47). In this work, we constrain

$$\gamma \in [0.5, 2.0], \qquad s \in [0, 5] \ \ (\text{equivalently } f_c \in [1, 10^5]\ \text{Hz}), \qquad a \geq 0,\ \ b \geq 0, \tag{53}$$

and set dataset-dependent upper bounds on (a, b) according to the measured PSD dynamic range. These constraints are implemented by mapping the network outputs to the feasible set via bounded activations and affine rescaling.

Unless otherwise stated, $E_{\boldsymbol{\phi}}$ is trained using local measurement patches to exploit spatial context, and then applied across the full field of view to produce parameter maps. For the SIMSI datasets in this work, we use patch size $h = w = 8$ and mini-batch size 32.

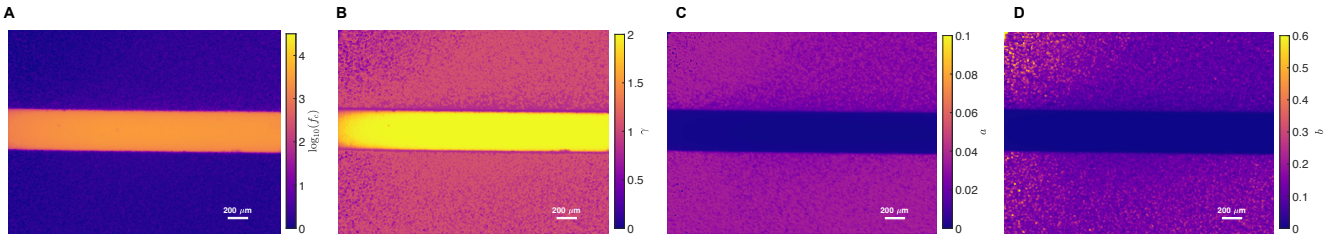

Fig. S2. Representative SIMSI PSD-parameter maps from the controlled-flow experiment. Maps of (A) $\log_{10}(f_c)$ (with f_c in Hz), (B) γ, (C) a, and (D) b inferred from the same SIMSI dataset using the estimator summarized in Sections S2.2-S2.3. The PSD was parameterized as $\mathcal{P}_I(f) = a\Big(1 + (f/f_c)^{\gamma}\Big)^{-1} + b$ (Eq. (47)), with $f_c = 10^s$. Scale bars, 200 μm.

S2.4. Reported parameter maps. For completeness, Fig. S2 reports representative maps of all inferred parameters (a, b, γ, f_c); for visualization, f_c is displayed as $\log_{10}(f_c)$. In the main text, we emphasize $f_c(\mathbf{r})$ because it provides a compact, interpretable flow-related index for the biological demonstrations, while (a, b, γ) capture additional aspects of the measured PSD shape.

S3. Comparison with MESI and 2P-MESI under photon-sufficient and photon-limited operation

This section provides a direct experimental comparison of SIMSI with two established camera-based speckle-visibility approaches: conventional MESI (5) and two-pulse modulation method (2P-MESI (2)). All three methods measure speckle-visibility statistics using the same optical geometry and flow phantom; the comparison isolates the role of within-exposure modulation and photon budget.

S3.1. Controlled-flow phantom and acquisition regimes. We imaged the same microfluidic flow phantom described in the main text, spanning imposed flow velocities of 0.21–10.42 mm/s. For each velocity, we acquired datasets using MESI, 2P-MESI, and SIMSI with matched optics, imaging geometry, camera settings, and reconstruction regions of interest (ROI). We considered two operating regimes:

- **Photon-sufficient regime:** unattenuated illumination, for which the measured photon rate was sufficient for all three methods to produce well-posed speckle-visibility estimates and stable fitted flow indices.
- **Photon-limited regime:** illumination reduced by inserting a neutral-density (ND) filter upstream of the AOM, resulting in an ∼18× reduction in measured optical power at the AOM input in our implementation. We emphasize that the controlled variable is the detected photon rate per estimate (and the corresponding proximity to the detector/digitization floor), rather than the absolute power value, which is system dependent.

Photon-limited operation is practically relevant whenever the detected photon rate must be reduced or is intrinsically low, including (but not limited to) cases in which irradiance must be limited for safety/thermal considerations, attenuation is high due to increased optical path length and scattering/absorption, or available optical power is constrained in compact/portable implementations.

S3.2. Duty-cycle and equalization under a peak-irradiance constraint. A central distinction among the three methods in photon-limited operation is the fraction of the exposure during which useful photons are collected for estimating the speckle-visibility statistic, under a fixed *peak* deliverable irradiance (i.e., without increasing peak power to compensate for low duty cycle). Let $I(t)$ denote the incident intensity at the AOM input and let $m(t) \in [0, 1]$ denote the within-exposure transmission/modulation waveform, so that $I_m(t) = I(t)m(t)$ is the detected intensity. The expected photon count per exposure satisfies

$$\bar{N}(T) \;\propto\; \int_0^T \langle I_m(t)\rangle \, dt. \tag{54}$$

Approximating $\langle I(t)\rangle = \langle I\rangle$ as constant over an exposure gives $\bar{N}(T) \propto \langle I\rangle \int_0^T m(t)\,dt = \langle I\rangle\, T\, \langle m\rangle_T$, where $\langle m\rangle_T = \frac{1}{T}\int_0^T m(t)\,dt$.

- **SIMSI:** $m(t) = \frac{1}{2} + \frac{1}{2}\cos(2\pi f_m t)$, so $\langle m\rangle_T = \frac{1}{2}$ under the integer-cycle condition used in this work, yielding

$$\bar{N}_{\text{SIMSI}} \;\propto\; \langle I\rangle \, \frac{T_S}{2}, \tag{55}$$

  where T_S is the SIMSI exposure.

- **2P-MESI:** two rectangular pulses of width τ_p per exposure give $\int_0^T m(t)\,dt = 2\tau_p$, hence

$$\bar{N}_{\text{2P-MESI}} \;\propto\; \langle I\rangle \, (2\tau_p). \tag{56}$$

- **MESI:** MESI requires measurements across multiple exposure times with the *mean recorded intensity* approximately equalized across exposures to avoid confounding $K^2(T)$ with exposure-dependent photon statistics and noise contributions. In our implementation, equalization is performed by setting the AOM transmission to a constant factor $\alpha(T)$ within each exposure, i.e., $m(t) = \alpha(T)$, with $\alpha(T_{\min}) = 1$ (the shortest exposure sets the reference under the peak-irradiance cap) and $\alpha(T) \le 1$ for longer exposures. Then

$$\bar{N}_{\text{MESI}}(T) \;\propto\; \langle I\rangle \, \alpha(T)\, T, \qquad \alpha(T) \approx \min\{1,\, T_{\min}/T\}, \tag{57}$$

  so the equalized sequence has $\bar{N}_{\text{MESI}}(T) \approx \langle I\rangle\, T_{\min}$. Consequently, if $\langle I\rangle T_{\min}$ lies near the detector/read-noise and 8-bit digitization floor, the *entire equalized MESI dataset* becomes photon-starved, and the speckle-contrast estimator (which normalizes by a mean intensity near zero) can yield inflated values and/or NaNs.

For reference, under matched peak irradiance and camera settings, the photon-count ratio between SIMSI and 2P-MESI is

$$\frac{\bar{N}_{\text{SIMSI}}}{\bar{N}_{\text{2P-MESI}}} = \frac{(T_S/2)}{2\tau_p} = \frac{T_S}{4\tau_p}. \tag{58}$$

With $T_S = 40$ ms and $\tau_p = 15$ μs, $\bar{N}_{\text{SIMSI}}/\bar{N}_{\text{2P-MESI}} \approx 6.7 \times 10^2$. For MESI, because the reference level is set by $T_{\min}$ under the peak-irradiance cap, matching SIMSI's per-estimate photon count using $T_{\min} = 50$ μs would require an $\mathcal{O}(T_S/(2T_{\min})) \approx 4 \times 10^2$ increase in peak irradiance.

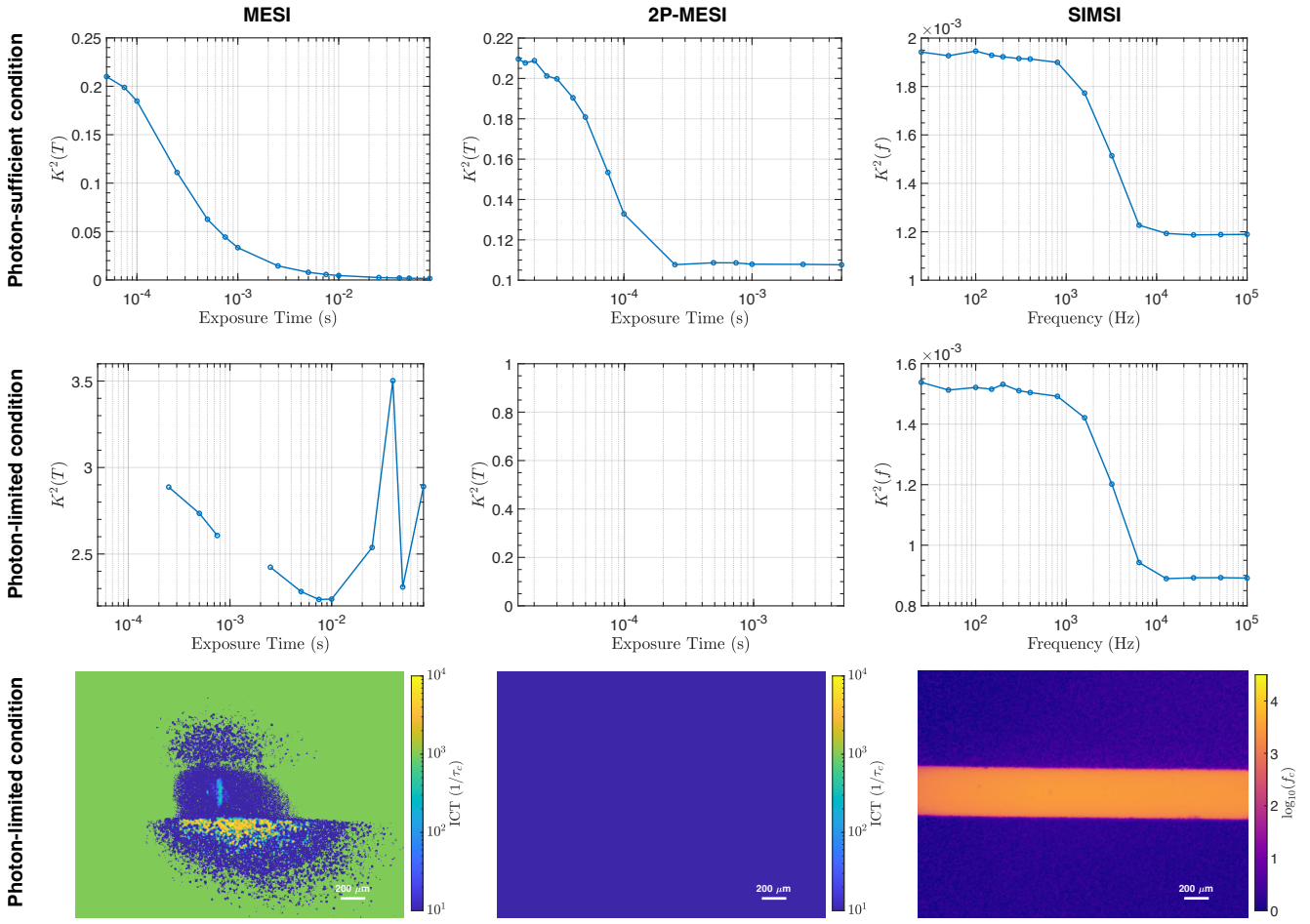

Fig. S3. Representative measurements and maps comparing MESI, 2P-MESI, and SIMSI under photon-sufficient and photon-limited conditions in the controlled-flow phantom. Top row: photon-sufficient regime (unattenuated illumination). Middle row: photon-limited regime (ND attenuation upstream of the AOM). Columns show MESI $K^2(T)$ curves (left), 2P-MESI $g_2(\tau)$ curves (middle), and SIMSI PSD measurements (right) from the same channel ROI. Bottom row: corresponding flow-index maps estimated from the photon-limited dataset. In the photon-limited regime, the raw frames are dominated by zeros with sparse single-count pixels (8-bit digitization), bringing the mean intensity near the digitization floor; MESI K^2 estimates can therefore become ill-conditioned (inflated values and NaNs), and 2P-MESI does not yield a valid $g_2(\tau)$ estimate in this dataset.

S3.3. Representative curves and maps. Figure S3 shows representative measurements from the same channel ROI under photon-sufficient and photon-limited regimes. In the photon-sufficient regime, all three methods produce physically plausible curves and spatially coherent flow-index maps. In the photon-limited regime, the raw speckle frames are dominated by zero-valued pixels with sparse single-count pixels (8-bit digitization), so the mean intensity approaches the digitization floor. Under these conditions, MESI contrast estimates become ill-conditioned (normalization by a near-zero mean), leading to inflated/nonphysical K^2 values and NaNs at some exposure points; similarly, the pulse-gated 2P-MESI frames do not provide sufficient photon counts to form a valid $g_2(\tau)$ estimate in this dataset. In contrast, SIMSI continues to provide usable PSD samples and coherent flow-index maps.

S3.4. ROI-averaged indices versus imposed flow speed. Figure S4 summarizes the same experiment by plotting ROI-averaged flow-related indices as a function of imposed flow velocity. In the photon-sufficient regime, all three methods show strong linear relationships with flow speed, with $R^2 = 0.9978$ (MESI), $R^2 = 0.9990$ (2P-MESI), and $R^2 = 0.9986$ (SIMSI). In the photon-limited regime, MESI and 2P-MESI do not yield valid ROI-averaged indices in this dataset because the underlying contrast estimates contain NaNs; SIMSI continues to provide well-defined f_c estimates with $R^2 = 0.9972$.

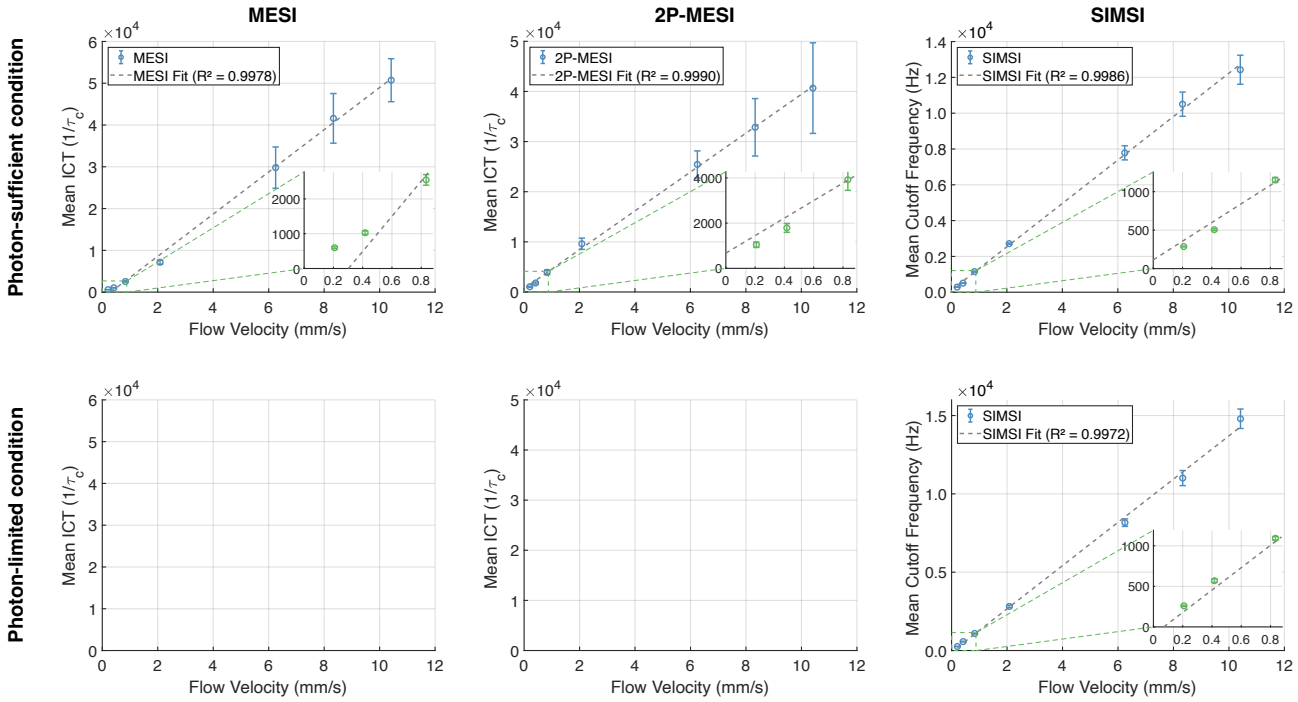

Fig. S4. ROI-averaged flow-related indices versus imposed flow speed in the controlled-flow phantom. Top row (photon-sufficient): MESI and 2P-MESI report inverse correlation time (ICT) and SIMSI reports cutoff frequency f_c; linear fits give $R^2 = 0.9978$ (MESI), $R^2 = 0.9990$ (2P-MESI), and $R^2 = 0.9986$ (SIMSI). Bottom row (photon-limited): SIMSI continues to provide well-defined f_c estimates with $R^2 = 0.9972$ (right), whereas MESI and 2P-MESI do not yield valid ROI-averaged indices in this dataset because the underlying contrast estimates contain NaNs (left and middle omitted). Error bars denote ROI variability.

References

1. M Siket, I Jánoki, K Demeter, M Szabó, P Földesy, Time varied illumination laser speckle contrast imaging. *Opt. Lett.* **46**, 713–716 (2021).
2. Q Fang, A Tomar, AK Dunn, Wide-field intensity fluctuation imaging. *Biomed. Opt. Express* **15**, 1004–1020 (2024).
3. AK Dunn, H Bolay, MA Moskowitz, DA Boas, Dynamic imaging of cerebral blood flow using laser speckle. *J. Cereb. Blood Flow Metab.* **21**, 195–201 (2001).
4. DA Boas, AK Dunn, Laser speckle contrast imaging in biomedical optics. *J. Biomed. Opt.* **15**, 011109–011109 (2010).
5. AB Parthasarathy, WJ Tom, A Gopal, X Zhang, AK Dunn, Robust flow measurement with multi-exposure speckle imaging. *Opt. Express* **16**, 1975–1989 (2008).
6. H Lu, J Ashbrook, AK Dunn, Label-free, physics-constrained learning for multi-exposure speckle imaging parameter estimation. *bioRxiv* (2026).